Nanostructured Hybrid Silicon/Carbon Nanotube Heterostructures: Reversible High-Capacity Lithium-Ion Anodes

Wei Wang[†,§] and Prashant N. Kumta[†,‡,*]

[†]Department of Mechanical Engineering and Materials Science, University of Pittsburgh, Pittsburgh, Pennsylvania 15261 and [‡]Departments of Bioengineering and Chemical and Petroleum Engineering, University of Pittsburgh, Pittsburgh, Pennsylvania 15261. [§]Present address: Pacific Northwest National Laboratory, Richland, Washington 99352.

ABSTRACT Lithium-ion batteries have witnessed meteoric advancement the last two decades. The anode area has seen unprecedented research activity on Si and Sn, the two anode alternatives to currently used carbon following the initial seminal work by Fuji on tin oxide nanocomposites. Recent reports on silicon nanowires, porous Si, and amorphous Si coatings on graphite nanofibers (GNF) have been very encouraging. High capacity and long cycle life anodes are still, however, elusive and much needed to meet the ever increasing energy storage demands of modern society. Herein, we report for the first time the synthesis of novel 1D heterostructures comprising vertically aligned multiwall CNTs (VACNTs) containing nanoscale amorphous/nanocrystalline Si droplets deposited directly on VACNTs with clearly defined spacing using a simple two-step liquid injection CVD process. A hallmark of these single reactor derived heterostructures is an interfacial amorphous carbon layer anchoring the nanoscale Si clusters directly to the VACNTs. The defined spacing of nanoscale Si combined with their tethered CNT architecture allow for the silicon to undergo reversible electrochemical alloying and dealloying with Li with minimal loss of contact with the underlying CNTs. The novel heterostructures thus exhibit impressive reversible stable capacities ∼2050 mAh/g with very good rate capability and an acceptable first cycle irreversible loss ∼20% comparable to graphitic anodes indicating their promise as high capacity Li-ion anodes. Although warranting further research, particularly with regard to long-term cycling, it can be envisaged that optimization of this simple approach could lead to reversible high capacity next generation Li-ion anodes.

KEYWORDS: silicon · carbon nanotube · anode · lithium battery

Modern technology driven society relies largely on vehicles for transportation and the use of high technology devices. This high technology base combined with automation and the impending need to protect the environment from the large volume of greenhouse gas and other toxic emissions known to be ecologically hazardous has placed stringent demands on the need to have high performance consumer and portable electronic devices. The portable nature of these devices makes it even more necessary to have rechargeable batteries that can provide higher energy densities and longer cycle life prolonging the use of battery operated devices before recharging the batteries. Lithium-ion batteries since the commercialization of the first generation batteries by Sony in 1991 have emerged on the forefront of rechargeable batteries. Despite two decades of intense research, the search for high performance rechargeable lithium ion systems exhibiting higher energy density and longer service life to power an increasing diverse range of complex, fast performing, multifunctional electronic devices still continues.[1] In recent years, silicon has attracted considerable attention as a potential Li-ion battery anode material to replace the current graphite anode due to its high capacity (specific capacity of 4200 mAhg^{-1} corresponding to the $Li_{22}Si_5$, the maximum lithium containing alloy phase in the Li−Si system). Furthermore, the large abundance of silica mineral deposits worldwide makes silicon an ideal choice element from both the cost and the elemental reserves point of view.[2,3] However, the commercial application of the silicon anode in current lithium-ion batteries is hindered by the rapid capacity decay during cycling because of the enormous volume changes associated with the various phase transitions known to occur during the lithium alloying and dealloying processes resulting in decrepitation of the particles comprising the electrode finally leading to electrode failure.[2,4−8] Several strategies have been explored in recent years to overcome this problem;[3,9] prime examples include reducing the particle size,[10−12] fabrication of silicon containing composites,[13−16] and the generation of thin films of elemental silicon.[17,18] However, despite all of these advances, the systems studied exhibit only limited improvement in capacity and capacity retention. There is still a critical need for identifying methods to generate Si-based anodes exhibiting its intrinsic high energy density with good capacity retention, and reversibility.
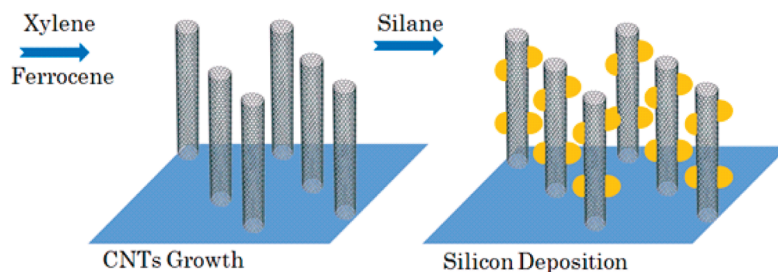
Figure 1. Schematic diagram showing the fabrication of silicon/carbon nanotube hybrid nanostructures using a liquid injection CVD to grow the initial vertically aligned CNTs followed by the subsequent deposition of silicon.

The burgeoning rise of nanotechnology has had a significant impact on various technologies including energy storage. In this regard, one-dimensional (1D) nanostructures have been of great interest for various applications due to their fascinating structure and unique properties.[19] An approach using 1D nanomaterials as lithium ion battery electrodes has been demonstrated with promising electrochemical properties for a number of systems such as Co_3O_4,[20−23] SnO_2,[24,25] TiO_2,[26] Fe_2O_3,[27] Ge,[28] nanowires, and $LiMn_2O_4$ nanorods.[29] In line with these recent reports, Cui *et al.* have recently developed silicon nanowire arrays, which have shown improved performance as lithium ion battery anode due to improved kinetics of lithium ion transport and facile strain relaxation.[30] However, these 1D nanomaterials are still prone to Coulombic efficiency limitations and efficient voltage independent cyclability not withstanding questions related to the large scale manufacturability and cost effectiveness of the process. They have also more recently reported deposition of silicon on commercially obtained carbon nanofibers (CNFs) exhibiting capacities in the range of ~2000 mAhg^{-1}.[31] However, a characteristic aspect of this approach is the fact that the silicon is deposited on carbon fibers that are initially coated onto the metal substrate, which in their case is stainless steel. The approach is indeed promising although the method could preferably allow for one-sided surface coverage of the carbon nanofibers due to the line of sight approach afforded by the initial surface coating of the carbon nanofibers. A feasible option would be the exploitation of the innovative materials chemistry route to design nanoscale hybrid structures with well-controlled size, crystallinity, and chemical composition to address all of the above different challenges. Recent development of coaxial nanowires/nanotubes have exhibited encouraging results, in which the 1D nanowire composite system has capitalized the specific electrochemical and physicochemical properties of the different components to exploit multiple functionalities brought about by axially or radially modulated compositions.[32−35]

Herein, we present for the first time a template-free, simple overarching generic design and fabrication of hybrid silicon/carbon nanotubes nanoscale heterostructures similar to the core−shell concept, in which the carbon nanotubes (CNTs) function as the core to af-

ford the mechanical strength and conductivity, while the silicon acts as the encompassing shell that can be tailored to form nanoclusters or thin layer coatings to deliver high capacity. Exploiting the combined merits of the mechanical and electrical properties of CNTs and the nanoscale attributes of nanostructured silicon would serve to address the challenging problem of decrepitation of the silicon electrode known to occur during cycling, while at the same time providing the desired high reversible capacity. This simple architecture can be easily extended to different active material systems, such as metal oxides, nitrides, and elemental metals of Sn and Ge. Cui and co-workers, as mentioned above, reported the crystalline−amorphous core−shell silicon nanowires in which the silicon core acts as a mechanical support and conducting pathway, while amorphous shells react with lithium.[36] Their recent report discussed above utilizes CNFs as the support matrix for enduring the expansion stresses of silicon.[31] Compared with crystalline silicon and carbon nanofibers, CNTs, however, are a better choice of core materials due to their superior mechanical strength[37] and outstanding kinetic transport of both electrons[38] and lithium ions.[39] Additionally, the unique nanoscale tubular morphology apart from their high aspect ratio, structural flexibility, and attractive tortuosity make them suitable to function as a nanoscale network to preserve the active particles in contact despite the phase-related pulverization of silicon.[40,41] The multiple facets of the unparallel properties of CNTs warrant a careful engineering of CNT-based 1D nanomaterials coupled with various forms of silicon to maximize their combined application as lithium ion battery anode materials.

RESULTS AND DISCUSSION

A simple two-step chemical vapor deposition (CVD) has been employed to prepare the hybrid silicon/carbon nanotubes (see Experimental Section for details) through a unified template-free approach shown in the schematic (Figure 1). The multiwalled carbon nanotubes (MWNTs) were first synthesized on bare quartz microscope slides using a liquid injection based CVD reactor,[42] in which xylene (C_8H_{10}) serves as the hydrocarbon source and iron from the decomposition of ferrocene ($Fe(C_5H_5)_2$) acting as a catalyst favoring the growth of MWNTs. The system is subsequently pumped
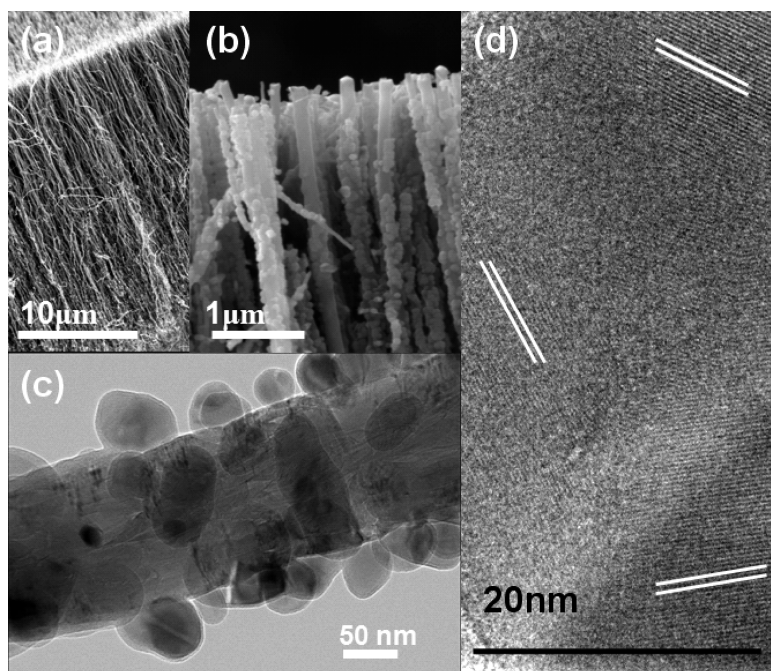
Figure 2. (a) SEM image of the aligned pristine carbon nanotubes prior to silicon deposition. (b) A low-magnification SEM image showing multiple clusters of carbon nanotubes covered with silicon nanoclusters. (c) TEM image of a single carbon nanotube covered with multiple silicon nanoclusters with spacing in between each other. (d) HR-TEM image showing different directions of the lattice fringes within a single silicon nanoparticle (white lines indicate the different lattice orientations).

down to deposit silicon onto MWNTs by a flow of SiH_4 gas. The hybrid silicon/carbon nanotubes are scraped off from the quartz slides to prepare the electrode for electrochemical evaluation. The Si/C ratio is determined by weighing the substrate before each deposition and is further controlled by the duration of reactions for MWNTs growth followed by silicon deposition, respectively. This provides the ability to tune the electrochemical properties of the hybrid silicon/carbon nanotubes. Under the experimental conditions used, the MWNT arrays grow perpendicular to the quartz substrates with an average growth rate ~25 μm/h estimated from SEM images. Figure S1 in the Supporting Information shows the silicon deposition rate.

One of the rationales for the design of Si/carbon nanotube hybrid nanostructure is the unique ability to grow aligned MWNTs covered with Si nanoclusters deposited directly on the CNTs as shown in Figure 1. Additionally, the growth conditions can be adjusted to grow the Si nanoclusters of various sizes on the CNT with each droplet separated from the other. The generation of Si droplets with defined spacing between each droplet is necessary to prevent the agglomeration of the silicon particles, particularly during cycling which would lead to particle growth ultimately resulting in the inability to curtail the mechanical stresses induced during cycling without pulverization. Figure 2b and c are the scanning electron microscopy (SEM) and transmission electron microscopy (TEM) images of the hybrid silicon/carbon nanotubes nanostructures, which distinctly show the silicon nanoclusters attached to the

individual carbon nanotubes at defined spacing between each other. As a comparison, the SEM image of the pristine aligned carbon nanotubes prior to silicon deposition is also shown in Figure 2a. The vertical alignment of the Si/CNTs hybrid nanostructure in Figure 2b is similar to that of CNTs shown in Figure 2a, which suggests that the overall configuration of the CNT forests remains intact after silicon deposition. The average tube diameter of the MWNTs is in the range of 40−50 nm. Larger and thinner tubes were also observed in the mix. It is clear that the carbon nanotube surface provide the desired sites for silicon particle to nucleate heterogeneously and grow during the subsequent SiH_4 decomposition step. Figure 2d is a high-resolution TEM (HR-TEM) image showing the different orientation of lattice fringes within a single silicon nanoparticle.

Figure 3a is a HR-TEM image showing a crystalline silicon nanocluster ~40 nm in diameter size adhered to a single carbon nanotube. It is evident from Figure 3a that a distinct interfacial layer is formed between the carbon nanotube and the silicon nanoparticle. The composition of the interfacial layer has been studied by conducting electron energy-loss spectroscopy (EELS) measurements on carbon nanotube, silicon nanoparticle, and the interface. EELS spectra collected at the carbon nanotube shown in Figure 3b demonstrate two peaks, one at 298 eV and the other at 325 eV, both of which are attributed to the energy loss peaks of π-bonds and σ-bonds of carbon.[43] On the other hand, at the center of the silicon nanoparticle, the EELS spectra collected matches well with that of $L_{2,3}$ edge for pure
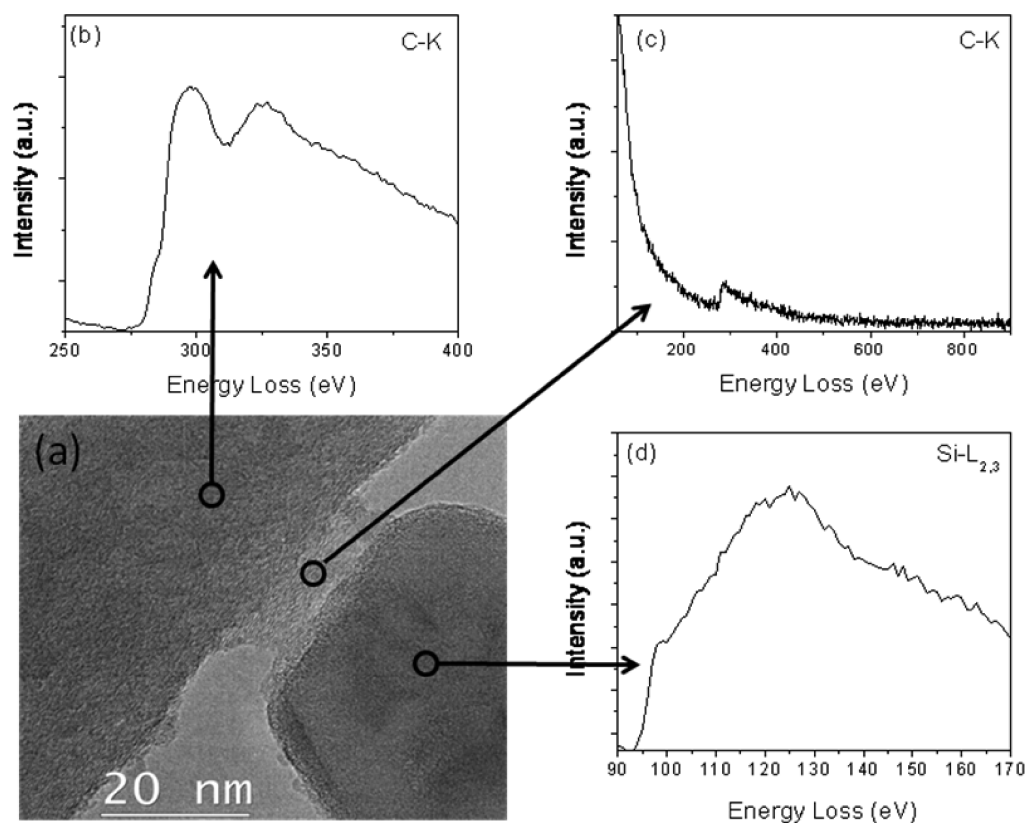
Figure 3. (a) HR-TEM image of a silicon nanoparticle that is grafted on the carbon nanotube. EELS spectra collected at (b) carbon nanotube, (c) interface, and (d) silicon nanoparticle.

silicon, which start at ~100 eV, followed by a broadened region.[44] It is also evident from Figure 3c that the EELS spectra acquired from the interfacial region between the silicon nanoparticle and carbon nanotube corresponds to that of amorphous carbon.[45] Apart from this amorphous carbon peak, there are no other peaks detected from the spot on the interface in Figure 3c. Furthermore, it should be noted that there is no peak at 103 eV characteristic of SiC eliminating its existence at the interface.[46] These results clearly indicate the presence of an amorphous carbon interlayer serving to tether the Si droplets to the underlying CNT. The anchoring of the Si nanoclusters to the underlying CNTs by the amorphous carbon interface layer will be a key factor contributing to maintaining the Si clusters in contact with the CNTs during electrochemical cycling discussed below.

The formation of the amorphous carbon interfacial layer is believed to be initiated at the beginning of the silicon deposition, in which the SiH_4 gas adsorbs onto the carbon nanotubes surface prior to its decomposition. Due to the high affinity between hydrogen and carbon atoms, it is likely that an initial condition favorable to the creation of a hydrogen−carbon surface between the carbon atoms on the carbon nanotube and the hydrogen atoms corresponding to the SiH_4 gas is created. The attachment of the SiH_4 gas droplet on to the CNT could very well act as a bridge to connect the carbon and silicon atoms during the subsequent de-

composition process, eventually resulting in the formation of the solid silicon nanoparticle. Due to the strong affinity of silicon and carbon to hydrogen, it is likely that intermediate complex moieties of -$[Si-H\cdots C]_n$ type species are formed. Because the growth temperature is very much below the thermodynamic temperature favorable for the formation of SiC, it is likely that the carbon separates out from the silicon−hydrogen−carbon complex to form the observed amorphous carbon interface layer. More detailed studies of the growth conditions would be needed to be conducted to validate the above hypothesis and ascertain the exact mechanism of formation of the amorphous carbon layer.

Although the exact mechanism of formation of the amorphous carbon interface is unclear at present, the formation of the interfacial bonding between carbon nanotube and the silicon nanoparticle appears to be a key factor contributing to the much improved electrochemical performance of the system by containing the active silicon particles to remain in contact during the lithium alloying and dealloying steps. On the other hand, the underlying carbon nanotube is expected to provide a facile pathway for the transportation of both electrons and lithium ions to/from the neighboring silicon nanoclusters acting as the lithium alloying and dealloying sites. The excellent electron and ion transfer kinetics associated with carbon nanotubes also contributes to the superior electrochemical performance of the system by lowering the internal resistance for both
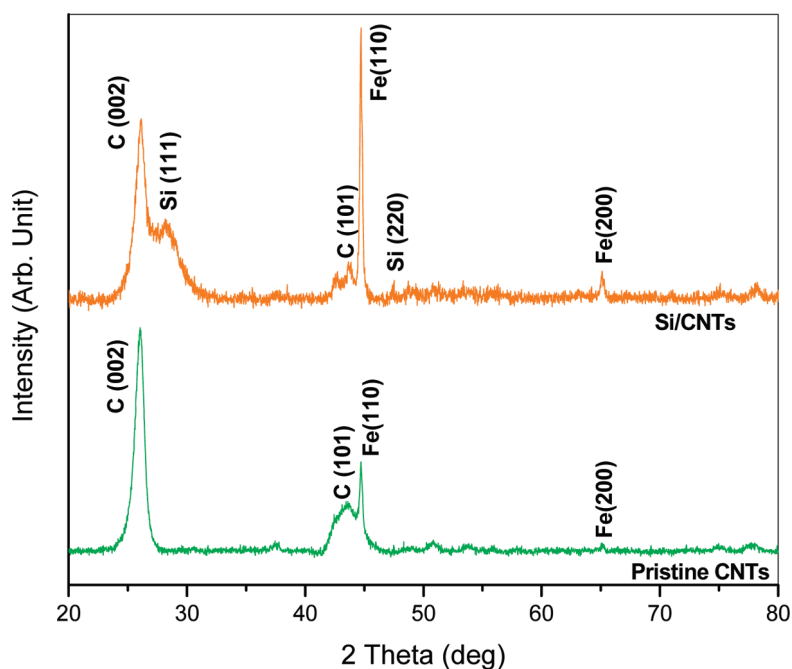
Figure 4. X-ray diffraction patterns of pristine CNTs and hybrid silicon/CNT nanostructures.

electrons and lithium ions to facilitate the dealloying reaction over the small surface area of silicon particles.[8]

X-ray diffraction (XRD) patterns of pristine CNTs and hybrid silicon/CNT nanostructures are shown in Figure 4. The presence of the nanocrystalline silicon characteristic peaks corresponding to the (111), (220) diffraction planes are observed. This is in good agreement with the HR-TEM image shown in Figure 2d, in which different orientations are identified by the differently oriented fringe patterns seen in a single silicon nanoparticle with a size of ~40 nm in diameter attached to the carbon nanotube. A peak at 26.4° attributed to the (002) plane of hexagonal graphite structure indicates the presence of CNTs. The existence of iron which is used to catalyze and seed the growth of CNTs from the decomposition of ferrocene is also confirmed by the Fe peak of (110) and (200), which is encapsulated inside the core channel of carbon nanotubes. The amount of iron present in the CNTs has been determined to be ~5.5% in weight by thermogravimetric analysis (TGA). The details are provided in the Supporting Information.

Following the generation of the CNTs and the deposition of silicon over the CNTs, the silicon/CNT nanostructures are scrapped off from the quartz substrate by a razor blade to mix the Si/CNT heterostructures with binder and carbon additives to prepare the electrodes for electrochemical cycling tests. The silicon/CNT film breaks into small pieces with the Si/CNT hybrid heterostructures lying flat on the Cu current collector following preparation of the electrode (SEM image of the electrode is supplied in the Supporting Information, Figure S3). Figure 5a shows the voltage profiles generated by the hybrid silicon/CNTs nanostructures anode after 1, 10, and 30 cycles. From the voltage profile, it can be

seen that the electrochemical lithiation and delithiation of the nanocrystalline silicon nanoparticles attached to the CNT surface is consistent with previous reports on silicon anodes,[30] in which a long flat plateau during the first discharge is observed. The onset of the silicon lithiation potential plateau at ~120 mV is indicative of the presence of crystalline silicon,[4] which confirms the presence of crystalline silicon evidenced in the HR-TEM images shown in Figure 2. Unlike the staging mechanism observed in graphite, there is no well-defined redox potential for lithium insertion/extraction with the CNTs. In Figure 5a, there is also no other potential plateau resolved other than the one corresponding to silicon.

The variation of specific gravimetric capacity with cycle number of the hybrid silicon/CNT nanostructures anode is shown in Figure 5b. The first discharge and charge capacities are 2552 and 2049 mAg^{-1}, respectively (all of the capacity values are calculated on the basis of silicon + CNT mass), with an initial Coulombic efficiency of 80.3%, corresponding to an irreversible capacity loss of 19.7%. In the subsequent cycle, the Coulombic efficiency however soon reaches 99% and remains relatively stable. An increase in both discharge and charge capacity is observed from the second cycle onward due to the activation of more silicon atoms actively reacting with lithium.[47] The composite anode remains stable during subsequent cycling exhibiting a fade rate of ~0.15%/cycle for the subsequent 25 cycles. Cycling data of the Si/CNTs nanostructures anode up to 100 cycles (supplied in Supporting Information) however indicate a rapid fade in capacity from 25 to 50 cycles (~1.3% fade per cycle between 25 and 50 cycles) when the capacity drops to ~1250 mAh/g, which then gradually stabilizes to ~1000 mAh/g (~0.4% capacity
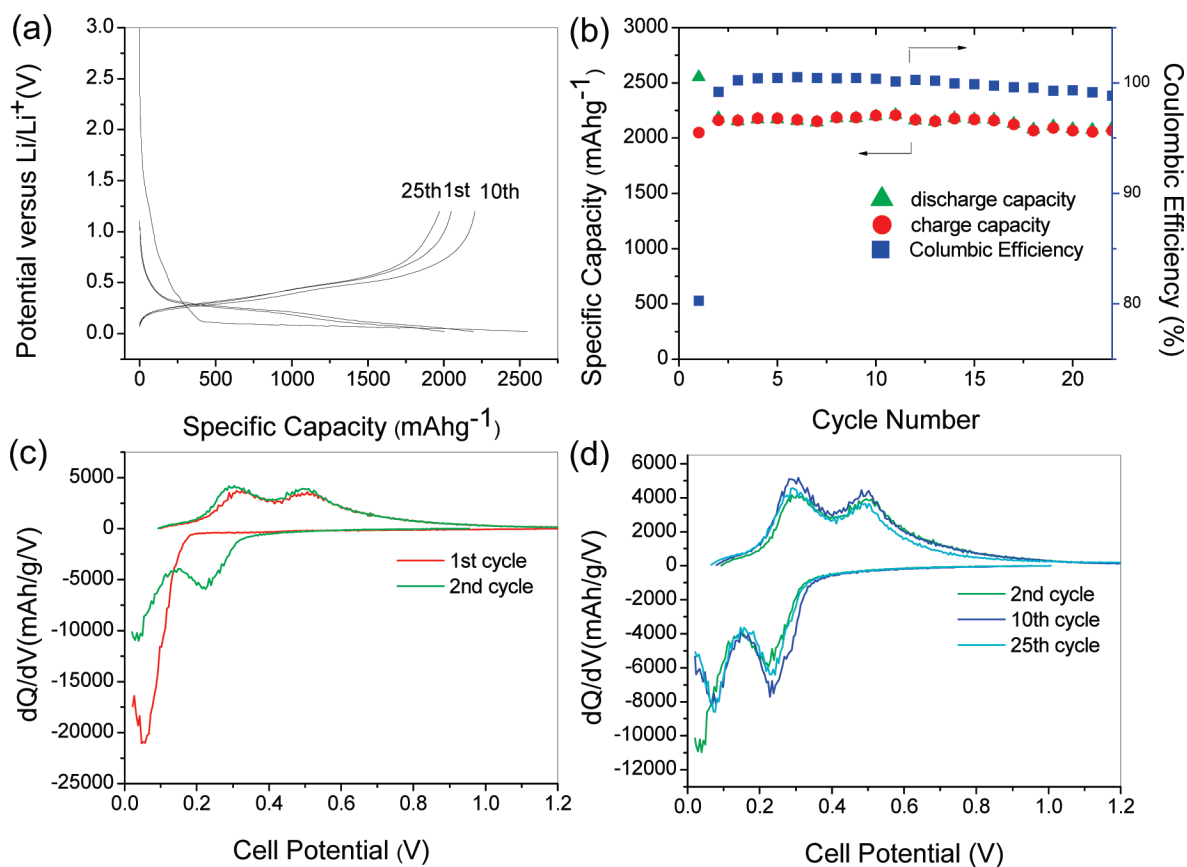
Figure 5. (a) Voltage profiles for hybrid silicon/CNT nanostructures anode after 1, 10, and 25 cycles. (b) Curve of discharge/charge capacity and Coulombic efficiency of the cell over 25 cycles. (c, d) Plots of differential capacity with cell potential of hybrid silicon/CNT nanostructures anode: (c) after 1st and 2nd cycle, (d) after 2nd, 10th, and 25th cycle. (All cells except the rate capability test are cycled at a current rate of 100 mAg^{-1} in the potential window of 0.02−1.2 V.)

fade rate from 50 to 100 cycles). The specific capacity of the Si/CNTs nanostructures anode remains ∼1000 mAh/g at the end of the 100th cycle. At ∼C/10 rate, retention of ∼1000 mAh/g indicates the promising nature of these vertically grown Si/CNT hybrid heterostructures. The reasons contributing to this drop in capacity is at present unknown but could relate to a number of factors such as: (1) weakening of the Si−CNT interface leading to detachment of the Si droplets from the CNT; (2) weakening of the solid electrolyte interface (SEI) layer leading to kinetic barriers for Li$^+$ transport; and (3) fragmentation of the Si droplets attached to the CNT following 25 cycles. Further detailed investigation into the causes contributing to the capacity fade during prolonged cycles after 25 cylces is warranted, which is currently under way. Nevertheless, the Si/CNTs hybrid anode demonstrate a capacity ∼1000 mAh/g even after 100 cycles at C/10 rate, which is ∼4-fold higher than the practical capacity achieved with graphite. The rate capability of the hybrid silicon/CNT nanocomposite was also analyzed. Figure 6 shows the charge and discharge curves observed at C/10, C/4, C/2, 1.3C, and 2.5C rates, demonstrating good cyclability. Even at a current rate of 2.5C, the capacity remained ∼1000 mAhg^{-1}, which is almost three times higher than the practical capacity obtained from graphite. This

excellent electrochemical performance of hybrid silicon/CNTs nanostructures as lithium-ion battery anode is thus attributed to its unique structure to prevent the agglomeration of silicon nanoparticles, the facile strain relaxation afforded by the CNTs and the formation of the interfacial amorphous carbon bond layer between the CNTs and silicon ensuring good contact of the silicon to CNT. Furthermore, the superior electrical and mechanical properties of CNTs, the desired kinetic transport response of lithium ions and electrons as well as the mechanical strength of the CNT help to anchor the active silicon atoms helping to achieve the superior performance that is not achievable using the traditional hitherto approaches reported in the literature.

The irreversible capacity usually originates from the formation of SEI layers due to the redox reaction of Li$^+$ with the electrolyte solvent molecules. The SEI formation has been correlated with the surface area of the carbon anode and it is reasonable to believe that similar mechanisms would apply to the CNTs in the present case.[48] The specific surface area of the pristine CNTs and the Si-CNTs composite were measured using the Brunauer−Emmett−Teller method, which is shown in Figure 7. The initial specific surface area of the pristine MWCNTs is ∼240 m^2 g^{-1}. A significant reduction in the specific surface area is observed after the deposition of

silicon. In addition, the specific surface area exhibits a linear relationship with increasing silicon content of the composite in general as shown in the inset of the Figure 7. Thus, it should be noted that due to the near complete coverage of the CNT area by silicon nanoclusters, the irreversible loss observed in this study is much lower than the irreversible losses in the range of 50% reported in our previous research,[41] in which single wall CNTs (SWCNTs) of high surface area are physically mixed with silicon and graphite powder without the presence of any interfacial layer between the CNTs and the silicon particles. The high surface area CNTs thus exposed to the Li^+ in the electrolyte results in first cycle irreversible losses of ~50%. Another potential contribution to the irreversible loss is the formation of SiO_x on the surface of the silicon nanoclusters. However, the reduction plateau of SiO is not observed in the voltage profile. More research is warranted to identify the reasons contributing to the reduced irreversible loss. Nevertheless, the observed irreversible loss of ~20% in the present heterostructures is thus comparable to those seen in graphitic anodes, adding to the potential promise of these novel heterostuctures as alternative anodes.

The plot of differential capacity with cell potential for the hybrid silicon/CNTs nanostructures is shown in Figure 5c,d. Upon close examination of the first discharge, a main peak is observed at 0.060 V with an onset potential of ~0.12 V during the first discharge corresponding to the long flat plateau in the first discharge voltage profile, which is widely considered by several researchers due to the formation of metastable Li–Si based amorphous phase (a-Li_xSi) by a solid state amorphization reaction, wherein the formation of crystalline intermetallic phases is denied due to the sluggish kinetics.[4,5,7,30,49] When cycled at an extremely slow rate of $C/100$, Li and Dahn reported the formation of $Li_{15}Si_4$ phase at ~60 mV during first discharge.[5] However, similar to Moni and Kumta's recent report,[49] this phase formation is not observed in this research, possibly due to the fact that the electrode was cycled at a moderate current rate (~$C/10$), which may likely bypass the formation of $Li_{15}Si_4$ phase. On the other hand, unlike the cycling behavior of the crystalline silicon during first charge, in which a sharp peak usually observed at ~0.45 V, indicating the formation of amorphous Si by the dealloying reaction, the differential capacity plot of the first charge (Figure 5c) shows not only a broad hump at ~0.45 V, but also an additional broad peak with a peak potential at ~0.3 V. A similar dQ/dV curve is usually observed for amorphous silicon thin films as well as for bulk amorphous silicon arising from the second charge onward.[7,49] From a recent report of Datta et al.,[49] it is suggested that the peak at ~0.3 V is due to
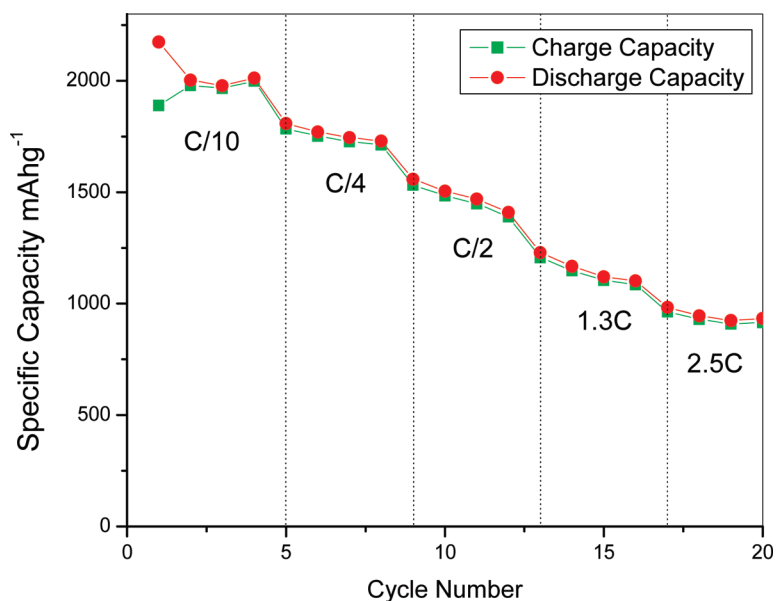

Figure 6. Specific capacity of hybrid silicon/CNT nanostructures anode cycled at different discharge and charge rates.

the dealloying of Li ions from the P–III phase (Li-24 atom %Si($Li_{3.17}$Si)) to P–II (Li-30 atom %Si(Li_7Si_3)) phase transition, and the 0.45 V peak corresponding to the transformation from P–II to P–I phase (Li-50 atom %Si(LiSi)). The fact that the two broad peaks are observed in the first charge suggests that the possibility of the presence of amorphous silicon in the present findings cannot be ruled out.

The differential capacity plots of the second and subsequent 10th and 25th cycle discharge and charge reactions of the hybrid Si/CNTs nanocomposite anode are shown in Figure 5c,d. Two peaks at ~0.23 and ~0.08 V appear during discharge in the subsequent 2nd, 10th, and 25th cycles, suggesting the process of dealloying from the P–I phase to form the P–II phase
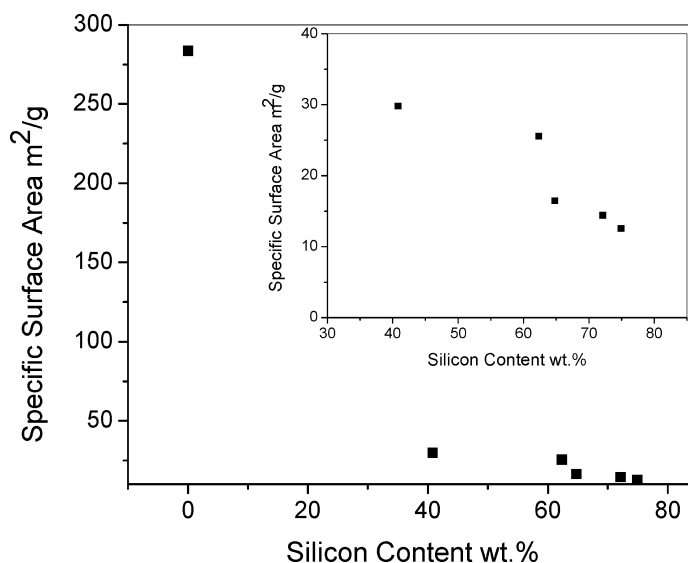

Figure 7. Specific surface area plotted against silicon content. The inset is a magnified view of the region where the silicon content ranges from 40–75 wt %.

and the subsequent transition from the P−II phase to form the P−III phase.[49] In addition, similar to the first discharge reaction, a peak at potential ~0.045 V is also observed during the second discharge due to the lithiation of crystalline silicon to form amorphous silicon suggesting a presence of crystalline and amorphous silicon in agreement to the XRD and HRTEM data discussed above. In Figure 5d, the magnitude of the peaks in the 10th cycle is the highest, which again as discussed before is due to the progressive activation of silicon.

CONCLUSIONS

In summary, a unique hybrid silicon/CNT 1D nanostructure involving silicon nanoclusters decorating the surface of the CNTs tethered to the CNTs *via* the formation of an interfacial amorphous carbon phase bonding is synthesized through a simple two-step CVD process. In this process, the carbon nanotubes are first synthesized vertically aligned on a quartz plate with defined spacing in between each other, which allows the silane gas to contact all the exposed surfaces of each individual carbon nanotube within the forest, resulting in a homogeneous deposition of silicon nanoclusters on the carbon nanotube surface. The CNT functions as a flexible mechanical support for strain release offering an efficient conducing channel, while the nanoclustered silicon provides the high capacity. It is demonstrated that the hybrid silicon/CNTs exhibit high reversible capacity of ~2000 mAhg^{-1} with very little fade in capacity of ~0.15% per cycle over 25 cycles. The proposed approach affords a very facile strategy for the fabrication of next generation anodes exhibiting high energy density and cycle life.

EXPERIMENTAL SECTION

Materials Synthesis. A two-stage CVD reactor comprising of liquid and gas injectors is employed for preparing MWNTs on bare quartz microscopy slides inside a quartz tube. Approximately 6.5 mol % of ferrocene was dissolved in xylene to obtain a feed solution with ~0.75 at. % Fe/C ratio, and is injected continuously into the two-stage tubular quartz reactor, comprising a preheater maintained at 200 and 750 °C for reactor, respectively. Ferrocene sublimes at ~190 °C and xylene has a boiling temperature of ~140 °C. The liquid exiting the capillary tube is immediately volatilized and swept into the reaction chamber by a flow of 200−1000 sccm of a mixture of ultrahigh purity argon (UHP-Ar) with 10% pure hydrogen. After the reaction, the preheater and the furnace were allowed to cool down in flowing argon.

Silicon deposition is performed in the same CVD furnace, where the pregrown CNTs with quartz slide is loaded at the center of hot zone. The reactor is pumped down to vacuum, purged with UHP-Ar gas then heated to desired temperatures. The deposition is carried out for different periods of time at temperatures ranging from 450 to 750 °C with a mixed flow of 20 sccm SiH$_4$ and a protective argon gas. The mass of the CNTs and silicon is accurately determined by measuring the mass of the substrate each time before and after the CNTs growth and silicon deposition using an analytical balance (Mettler Toledo AB135, 0.01 mg). The as-synthesized silicon/CNTs are then scraped off from the quartz substrate for characterization and electrochemical test.

Materials Characterization. The silicon/CNTs nanomaterial powders were characterized by X-ray diffraction (XRD) using Philips XPERT PRO system with Cu Kα (λ = 0.15406 nm) radiation to identify the phases present. SEM (Philips XL30 operating at 20 kV) was employed to investigate the microstructure of the as-synthesized nanomaterials. TEM and HRTEM are performed on Joel 2000EX and the FEI Tecnai F20 field emission transmission electron microscope equipped with an electron EELS system to observe the morphology, structure and particle size of the as-prepared nanomaterials. For TEM analysis, the silicon/CNTs nanomaterial powders were dispersed on 3.05 mm diameter copper grids (electron microscopy science) containing a holey carbon film in methanol by sonication followed by drying in a desiccator overnight. TGA of pristine CNTs was conducted using NETZSCH STA 409PC LUXX thermal analysis instrument. The heating rate was set at 10 K/min, which was conducted in dry air gas flow.

Electrochemical Test. The hybrid silicon/CNT nanomaterial electrodes were fabricated on copper substrate of approximately 10 mm diameter to evaluate the electrochemical characteristics primarily involving constant current cycling tests. A total of 50 wt % of the active powder, 10 wt % acetylene carbon black, and 40 wt % of sodium carboxymethyl cellulose binder dissolved in deionized water were mixed to produce a slurry that was then coated onto a copper foil and dried overnight at 383 K in a vacuum oven prior to assembling the customized test cell. A 2016 coin cell design was utilized for the electrochemical tests employing a lithium foil as the counter electrode and 1 M LiPF$_6$ in ethylene carbonate/dimethyl carbonate (2:1) as the electrolyte. All the batteries tested in this study were cycled from 0.02 to 1.2 V employing a constant current density of 100 mAg^{-1} and a minute rest period between the charge/discharge cycles using a potentiostat (Arbin electrochemical instrument).

Supporting Information Available: Silicon deposition rate, TGA to determine iron content inside CNTs, SEM image of the electrode, and long-term cycling data. This material is available free of charge *via* the Internet at http://pubs.acs.org.

REFERENCES AND NOTES

1. Armand, M.; Tarascon, J. Building Better Batteries. *Nature* **2008**, *451*, 652–657.
2. Boukamp, B. A.; Lesh, G. C.; Huggins, R. A. All-Solid Lithium Electrodes with Mixed-Conductor Matrix. *J. Electrochem. Soc.* **1981**, *128*, 725–729.
3. Kasavajjula, U.; Wang, C.; Appleby, A. Nano- and Bulk-silicon-based Insertion Anodes for Lithium-ion Secondary Cells. *J. Power Sources* **2007**, *163*, 1003–1039.
4. Obrovac, M. N.; Christensen, L. Structural Changes in Silicon Anodes during Lithium Insertion/Extraction. *Electrochem. Solid-State Lett.* **2004**, *7*, A93–A96.
5. Li, J.; Dahn, J. R. An In Situ X-Ray Diffraction Study of the Reaction of Li with Crystalline Si. *J. Electrochem. Soc.* **2007**, *154*, A156–A161.
6. Limthongkul, P.; Jang, Y.; Dudney, N. J.; Chiang, Y. Electrochemically-Driven Solid-State Amorphization in Lithium−Silicon Alloys and Implications for Lithium Storage. *Acta Mater.* **2003**, *51*, 1103–1113.
7. Hatchard, T. D.; Dahn, J. R. In Situ XRD and Electrochemical Study of the Reaction of Lithium with Amorphous Silicon. *J. Electrochem. Soc.* **2004**, *151*, A838–A842.

8. Ryu, J. H.; Kim, J. W.; Sung, Y.; Oh, S. M. Failure Modes of Silicon Powder Negative Electrode in Lithium Secondary Batteries. *Electrochem. Solid-State Lett.* **2004**, *7*, A306–A309.

9. Larcher, D.; Beattie, S.; Morcrette, M.; Edstrom, K.; Jumas, J.; Tarascon, J. Recent Findings and Prospects in the Field of Pure Metals as Negative Electrodes for Li-Ion Batteries. *J. Mater. Chem.* **2007**, *17*, 3759–3772.

10. Yang, J.; Winter, M.; Besenhard, J. O. Small Particle Size Multiphase Li-Alloy Anodes for Lithium-ion Batteries. *Solid State Ionics* **1996**, *90*, 281–287.

11. Li, H.; Huang, X.; Chen, L.; Wu, Z.; Liang, Y. A High Capacity Nano-Si Composite Anode Material for Lithium Rechargeable Batteries. *Electrochem. Solid-State Lett.* **1999**, *2*, 547–549.

12. Graetz, J.; Ahn, C. C.; Yazami, R.; Fultz, B. Highly Reversible Lithium Storage in Nanostructured Silicon. *Electrochem. Solid-State Lett.* **2003**, *6*, A194–A197.

13. Mao, O.; Turner, R. L.; Courtney, I. A.; Fredericksen, B. D.; Buckett, M. I.; Krause, L. J.; Dahn, J. R. Active/Inactive Nanocomposites as Anodes for Li-Ion Batteries. *Electrochem. Solid-State Lett.* **1999**, *2*, 3–5.

14. Timmons, A.; Todd, A. D. W.; Mead, S. D.; Carey, G. H.; Sanderson, R. J.; Mar, R. E.; Dahn, J. R. Studies of $Si_{1-x}C_x$ Electrode Materials Prepared by High-Energy Mechanical Milling and Combinatorial Sputter Deposition. *J. Electrochem. Soc.* **2007**, *154*, A865–A874.

15. Datta, M. K.; Kumta, P. N. Silicon and Carbon Based Composite Anodes for Lithium Ion Batteries. *J. Power Sources* **2006**, *158*, 557–563.

16. Wang, W.; Datta, M. K.; Kumta, P. N. Silicon-Based Composite Anodes for Li-Ion Rechargeable Batteries. *J. Mater. Chem.* **2007**, *17*, 3229–3237.

17. Maranchi, J. P.; Hepp, A. F.; Kumta, P. N. High Capacity Reversible Silicon Thin-Film Anodes for Lithium-Ion Batteries. *Electrochem. Solid-State Lett.* **2003**, *6*, A198–A201.

18. Maranchi, J. P.; Hepp, A. F.; Evans, A. G.; Nuhfer, N. T.; Kumta, P. N. Interfacial Properties of the a-Si/Cu: Active—Inactive Thin-Film Anode System for Lithium-Ion Batteries. *J. Electrochem. Soc.* **2006**, *153*, A1246–A1253.

19. Lieber, M. C.; Wang, Z. L. Functional Nanowires. *MRS Bull.* **2007**, *32*, 99–104.

20. Nam, K. T.; Kim, D.; Yoo, P. J.; Chiang, C.; Meethong, N.; Hammond, P. T.; Chiang, Y.; Belcher, A. M. Virus-Enabled Synthesis and Assembly of Nanowires for Lithium Ion Battery Electrodes. *Science* **2006**, *312*, 885–888.

21. Li, Y.; Tan, B.; Wu, Y. Mesoporous Co_3O_4 Nanowire Arrays for Lithium Ion Batteries with High Capacity and Rate Capability. *Nano Lett.* **2008**, *8*, 265–270.

22. Lou, X.; Deng, D.; Lee, J.; Feng, J.; Archer, L. Self-Supported Formation of Needlelike Co_3O_4 Nanotubes and Their Application as Lithium-Ion Battery Electrodes. *Adv. Mater.* **2008**, *20*, 258–262.

23. Shaju, K. M.; Jiao, F.; Debart, A.; Bruce, P. G. Mesoporous and Nanowire Co_3O_4 as Negative Electrodes for Rechargeable Lithium Batteries. *Phys. Chem. Chem. Phys.* **2007**, *9*, 1837–1842.

24. Park, M.; Wang, G.; Kang, Y.; Wexler, D.; Dou, S.; Liu, H. Preparation and Electrochemical Properties of SnO_2 Nanowires for Application in Lithium-Ion Batteries. *Angew. Chem., Int. Ed.* **2007**, *46*, 750–753.

25. Ying, Z.; Wan, Q.; Cao, H.; Song, Z. T.; Feng, S. L. Characterization of SnO_2 Nanowires as an Anode Material for Li-Ion Batteries. *Appl. Phys. Lett.* **2005**, *87*, 113108–3.

26. Armstrong, G.; Armstrong, A. R.; Bruce, P. G.; Reale, P.; Scrosati., B. TiO_2(B) Nanowires as an Improved Anode Material for Lithium-Ion Batteries Containing $LiFePO_4$ or $LiNi_{0.5}Mn_{1.5}O_4$ Cathodes and a Polymer Electrolyte. *Adv. Mater.* **2006**, *18*, 2597–2600.

27. Chen, J.; Xu, L.; Li, W.; Gou, X. A-Fe_2O_3 Nanotubes in Gas Sensor and Lithium-Ion Battery Applications. *Adv. Mater.* **2005**, *17*, 582–586.

28. Chan, C. K.; Zhang, X. F.; Cui, Y. High Capacity Li Ion Battery Anodes Using Ge Nanowires. *Nano Lett.* **2008**, *8*, 307–309.

29. Kim, D. K.; Muralidharan, P.; Lee, H.; Ruffo, R.; Yang, Y.; Chan, C. K.; Peng, H.; Huggins, R. A.; Cui, Y. Spinel $LiMn_2O_4$ Nanorods as Lithium Ion Battery Cathodes. *Nano Lett.* **2008**, *8*, 3948–3952.

30. Chan, C. K.; Peng, H.; Liu, G.; McIlwrath, K.; Zhang, X. F.; Huggins, R. A.; Cui, Y. High-performance Lithium Battery Anodes Using Silicon Nanowires. *Nat. Nanotechnol.* **2008**, *3*, 31–35.

31. Cui, L.; Yang, Y.; Hsu, C.; Cui, Y. Carbon-Silicon Core-Shell Nanowires as High Capacity Electrode for Lithium Ion Batteries. *Nano Lett.* **2009**, *9*, 3370–3374.

32. Kim, D.; Hwang, I.; Kwon, S. J.; Kang, H.; Park, K.; Choi, Y.; Choi, K.; Park, J. Highly Conductive Coaxial SnO_2-In_2O_3 Heterostructured Nanowires for Li Ion Battery Electrodes. *Nano Lett.* **2007**, *7*, 3041–3045.

33. Kim, H.; Cho, J. Superior Lithium Electroactive Mesoporous Si@Carbon Core-Shell Nanowires for Lithium Battery Anode Material. *Nano Lett.* **2008**, *8*, 3688–3691.

34. Meduri, P.; Pendyala, C.; Kumar, V.; Sumanasekera, G. U.; Sunkara, M. K. Hybrid Tin Oxide Nanowires as Stable and High Capacity Anodes for Li-Ion Batteries. *Nano Lett.* **2009**, *9*, 612–616.

35. Reddy, A. L. M.; Shaijumon, M. M.; Gowda, S. R.; Ajayan, P. M. Coaxial MnO_2/Carbon Nanotube Array Electrodes for High-Performance Lithium Batteries. *Nano Lett.* **2009**, *9*, 1002–1006.

36. Cui, L.; Ruffo, R.; Chan, C. K.; Peng, H.; Cui, Y. Crystalline-Amorphous Core-Shell Silicon Nanowires for High Capacity and High Current Battery Electrodes. *Nano Lett.* **2009**, *9*, 491–495.

37. Yu, M.; Files, B. S.; Arepalli, S.; Ruoff, R. S. Tensile Loading of Ropes of Single Wall Carbon Nanotubes and their Mechanical Properties. *Phys. Rev. Lett.* **2000**, *84*, 5552–5555.

38. Thess, A.; Lee, R.; Nikolaev, P.; Dai, H.; Petit, P.; Robert, J.; Xu, C.; Lee, Y.; Kim, S.; Rinzler, A.; Colbert, D.; Scuseria, G.; Tománek, D.; Fischer, J.; Smalley, R. Crystalline Ropes of Metallic Carbon Nanotubes. *Science* **1996**, *273*, 483–487.

39. Meunier, V.; Kephart, J.; Roland, C.; Bernholc, J. Ab Initio Investigations of Lithium Diffusion in Carbon Nanotube Systems. *Phys. Rev. Lett.* **2002**, *88*, 075506-1–075506-4.

40. Demczyk, B. G.; Wang, Y. M.; Cumings, J.; Hetman, M.; Han, W.; Zettl, A.; Ritchie, R. O. Direct Mechanical Measurement of the Tensile Strength and Elastic Modulus of Multiwalled Carbon Nanotubes. *Mater. Sci. Eng. A* **2002**, *334*, 173–178.

41. Wang, W.; Kumta, P. N. Reversible High Capacity Nanocomposite Anodes of Si/C/SWNTs for Rechargeable Li-Ion Batteries. *J. Power Sources* **2007**, *172*, 650–658.

42. Wang, W.; Yang, K.; Gaillard, J.; Bandaru, P.; Rao, A. Rational Synthesis of Helically Coiled Carbon Nanowires and Nanotubes through the Use of Tin and Indium Catalysts. *Adv. Mater.* **2008**, *20*, 179–182.

43. Yase, K.; Horiuchi, S.; Kyotani, M.; Yumura, M.; Uchida, K.; Ohshima, S.; Kuriki, Y.; Ikazaki, F.; Yamahira, N. Angular-Resolved EELS of a Carbon Nanotube. *Thin Solid Films* **1996**, *273*, 222–224.

44. Batson, P. E. Current Trends for EELS Studies in Physics. *Microsc. Microanal. Microstruct.* **1991**, *2*, 395–402.

45. Egerton, R. *Electron Energy-Loss Spectroscopy in the Electron Microscope*, 2nd ed.; Springer: New York, 1996.

46. Saint, J.; Morcrette, M.; Larcher, D.; Laffont, L.; Beattie, S.; Pérès, J. P.; Talaga, D.; Couzi, M.; Tarascon., J.-M. Towards a Fundamental Understanding of the Improved Electrochemical Performance of Silicon-Carbon Composites. *Adv. Funct. Mater.* **2007**, *17*, 1765–1774.

47. Green, M.; Fielder, E.; Scrosati, B.; Wachtler, M.; Moreno, J. S. Structured Silicon Anodes for Lithium Battery Applications. *Electrochem. Solid-State Lett.* **2003**, *6*, A75–A79.

48. Salver-Disma, F.; Lenain, C.; Beaudoin, B.; Aymard, L.; Tarascon, J. Unique Effect of Mechanical Milling on the Lithium Intercalation Properties of Different Carbons. *Solid State Ionics* **1997**, *98*, 145–158.

49. Datta, M. K.; Kumta, P. N. In Situ Electrochemical Synthesis of Lithiated Silicon-carbon Based Composites Anode Materials for Lithium Ion Batteries. *J. Power Sources* **2009**, *194*, 1043–1052.